Acoustic Observation, Identification, and Scattering Intensity Measurement of Cold Seep Based on Bubble Resonance

Lin Guo, Octavian Postolache, *Senior Member, IEEE*, Lin Ma, and Yang Shi

***Abstract*— The active "cold seep" is indisputable evidence to identify the existence of submarine gas hydrate. Due to the difference in acoustic properties between cold seep bubbles and surrounding seawater, measuring scattering intensity is a new means to detect active cold seep. Cold seep bubbles are the main cause of acoustic scattering, and the scattering ability is closely related to the frequency of the incident sound wave, the radius of the bubble, and the depth of the bubble. This article introduces a ship-borne cold seep sonar system, which uses the resonance principle of bubbles to measure the scattering intensity at various depths underwater and display it with an intuitive acoustic image. Through the investigation and measurement of the cold seep located in the South China Sea, it is proven that the cold seep sonar system can well identify the submarine cold seep. The measured data are consistent with the theoretical simulation results, confirming that the cold seep bubbles have frequency-selective characteristics for incident sound waves. Compared with other detection methods, it has the characteristics of lossless, fast, and high efficiency.**

***Index Terms*— Acoustic resonance, cold seep identification, cold seep sonar system, scattering intensity measurement.**

I. Introduction

THERE are abundant, clean, and efficient natural gas hydrates distributed on the seafloor, which have extremely high resource value and have been the hotspot of long-term research [1]. The methane formed by the decomposition of natural gas hydrate infiltrates or spills into the overlying water in the form of gas, forming a gas column in seawater, which can characterize and discover the existence of gas hydrate. The cold seep is the area on the seafloor where natural gas hydrate-rich fluid seeps into the water layer. Compared with the surrounding seawater, it has unique physical characteristics, and the temperature does not increase significantly, so it is named "cold seep" [2]. When the gas source is sufficient, the methane gas will form the "bubble plume," which is a significant feature to prove the existence of submarine cold seep [3]–[5].

Acoustics has a natural advantage in underwater engineering applications [6]. Sound waves are scattered to all directions in the process of propagation when meeting the medium is inhomogeneous. Considering that there are differences in acoustic properties between "cold seep" and the surrounding seawater [7], active acoustic detection becomes an effective method for the identification of the seabed cold seep. The cold seep bubbles are the main cause of acoustic scattering, so the active cold seep can be observed by detecting the escaping bubbles from the cold seep. Liu *et al.* [8], Klaucke *et al.* [9], [10], Jones *et al.* [11], and Dumke *et al.* [7] identified and discussed the morphological characteristics of shallow gas related to gas leakage according to sea-bottom profile, seismic profiles, multibeam echo sounders, side-scan sonar, and so on that is mainly manifested as abnormal spots or linear reflections under the image. Tu *et al.* [12] verified that underwater bubbles with different depths damp the impact signal according to the bubble resonance theory.

To observe and identify cold seep on seafloor more intuitively, the ship-borne cold seep sonar system is designed in this article by using the characteristics of the bubble scattering and absorbing of the incident sound wave [13], [14]. After the sonar completes the measurement of the preset trajectory, the acoustic image is generated based on the scattering intensities of different underwater depths, which can realize the purpose of identifying the cold seep visually. Considering that the scattering intensity of the bubble is mainly determined by its resonance frequency [15]. According to the derivation, the resonance frequency of the bubble is related to its radius and depth [16], which directly affects the acoustic characteristic of the bubble. Therefore, to verify the feasibility of the ship-borne cold seep sonar, experimental verification is carried out. The experimental results under different incident frequencies are compared with the simulation results. It can be seen that the variation trend of the bubble scattering characteristic is consistent, which can verify the feasibility of

Manuscript received 14 April 2022; revised 24 May 2022; accepted 21 June 2022. Date of publication 11 July 2022; date of current version 20 July 2022. This work was supported by the Key Area Research and Development Program of Guangdong Province under Grant 2020B1111520001. The Associate Editor coordinating the review process was Alvaro Hernandez. *(Corresponding author: Yang Shi.)*

Lin Guo and Yang Shi are with the Acoustic Science and Technology Laboratory, Harbin Engineering University, Harbin 150001, China, also with the Key Laboratory of Marine Information Acquisition and Security, Ministry of Industry and Information Technology, Harbin Engineering University, Harbin 150001, China, also with the College of Underwater Acoustic Engineering, Harbin Engineering University, Harbin 150001, China, and also with the Shanghai Acoustics Laboratory, Chinese Academy of Sciences, Shanghai 201815, China (e-mail: guolin36@163.com; shiyang@mail.ioa.ac.cn).

Octavian Postolache is with the Instituto de Telecomunicações, 1049-001 Lisbon, Portugal, and also with the Department of Information Science and Technology, ISCTE-Instituto Universitário de Lisboa, 1649-021 Lisbon, Portugal (e-mail: opostolache@lx.it.pt).

Lin Ma is with the Shanghai Acoustics Laboratory, Chinese Academy of Sciences, Shanghai 201815, China (e-mail: malin_n@163.com).

Digital Object Identifier 10.1109/TIM.2022.3189634

the cold seep sonar system based on the scattering intensity measurement.

II. Measuring Principle

The bubble in water can be regarded as a cavity. When the sound wave contacts the bubble during propagation, a strong scattering process occurs. After the sound wave passes through the bubble group, its intensity decreases significantly. Burdick and William [17] and Urick [18] gave the conclusion: when the sound wave frequency is close to the resonance frequency, the scattering cross section is the largest, the target intensity is the strongest, and the bubbles are most easily detected.

A. Theoretical and Numerical Results

Assuming that the bubble medium and the biological medium are homogeneous, the other abiotic scattering sources can be ignored [18]. The small bubble is approximately uniformly deformed under the action of sound waves, and the scattering power of a single bubble can be obtained from the single bubble. From the scattering power, the scattering cross section of the bubble is [4], [7], [9]

$$\sigma_s = \frac{4\pi r^2}{\left\{\left[\left(\frac{0.33}{r}\sqrt{1+0.1d}\right)^2/f^2\right]-1\right\}^2+\delta^2} \tag{1}$$

where r is the radius of the bubble, d is the depth of the bubble, f is the incident frequency of the sound wave, and δ is the damping constant of the bubble vibration. The target intensity TS of a single bubble is

$$\mathrm{TS} = \begin{cases} 10\lg\dfrac{r^2}{\delta^2}, & f = f_0 \\ 10\lg\dfrac{r^2}{\left[\left(0.33\sqrt{1+0.1d}/r\right)^2/f^2-1\right]^2+\delta^2}, & \text{else.} \end{cases} \tag{2}$$

It can be seen from (2) that the target intensity of the bubble can reach the maximum value when the sound wave incident frequency $f = f_0$.

The target intensity of bubbles in water is simultaneously affected by the size of the bubble, its depth, and the frequency of the incident acoustic wave. Under the premise that the incident signal type is a single frequency, Fig. 1 shows the curve of the bubble scattering intensity as a function of the bubble radius and depth under different incident frequencies. It can be seen that with the increase of the incident frequency, the scattering intensity is gradually less affected by the bubble depth and size and gradually tends to be stable.

Furthermore, for different incident frequencies, there will have a corresponding size of the bubble that resonates with the sound wave, and the target scattering intensity can reach the maximum. When the sound wave frequency is lower than the resonance frequency, the scattering intensity decreases rapidly with the fourth power of the resonance frequency; when the sound wave frequency is higher than the resonance frequency, the scattering intensity decreases by about -10 dB and then tends to be stable. For the same incident frequency,

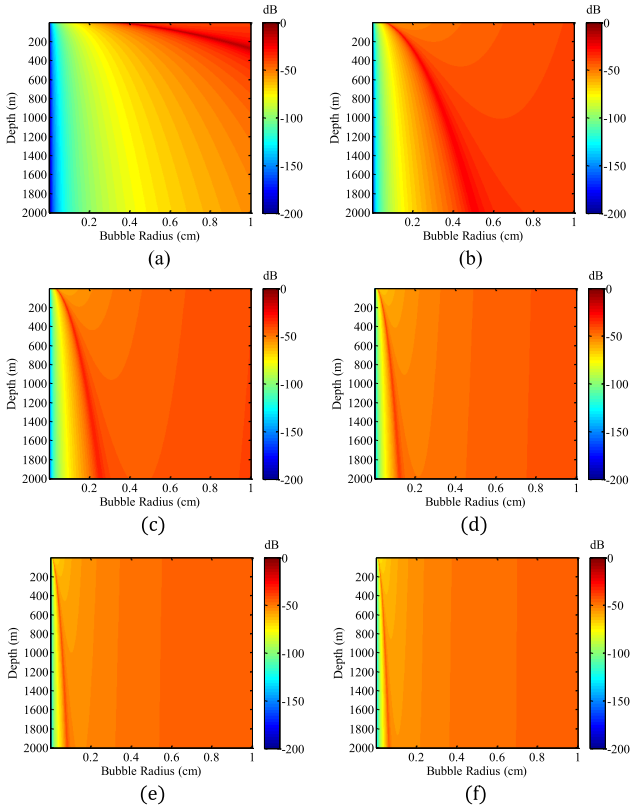

Fig. 1. Heatmap of bubble scattering intensity as a function of radius and depth under different incident frequencies. (a) $f = 1$ kHz. (b) $f = 5$ kHz. (c) $f = 10$ kHz. (d) $f = 20$ kHz. (e) $f = 30$ kHz. (f) $f = 40$ kHz.

as the depth increases, the bubble size of the resonance increases, while the resonance peak of the scattering intensity value becomes smoother.

B. Scattering Intensity Measurement

There are generally three types of measurement of bubble scattering intensity in seawater: theoretical model calculation method, direct measurement method [19], and inversion method using reverberation data. The theoretical model and the empirical formula used to calculate the scattering intensity of bubbles have been given in Section II-A. The direct measurement method is based on the definition of scattering intensity and the actual measured value of the scattering intensity. The method is often used in the laboratory, but it is not suitable for cold spring bubbles of the deep seafloor. The inversion method using reverberation data is also discussed in [20]. Many scholars, such as [19] and [21]–[24], have also done a lot of research work, numerical simulation, and experimental verification on the inversion of seafloor scattering intensity from the reverberation data. The scattering intensity is measured using the reverberation data inversion in this article.

The equivalent plane wave reverberation level is defined to measure the strength of the reverberation. When a plane wave of intensity I_s is incident on the hydrophone in the axial direction, the output voltage is equal to the voltage that the acoustic axis, which is placed in the reverberant sound field, is facing the target. Therefore, the intensity of the reverberation sound field is considered to be I_s. The reverberation level of

TABLE I
PARAMETER DEFINITION

Parameter	Definition
RX (dB)	Echo level of the transducer array
SRX (dB)	Receiving sensitivity of the transducer array
G (dB)	Receiver gain
SL (dB)	Source level of the acoustic emission signal
α	Acoustic absorption coefficient in seawater
λ (m)	Wavelength of the incident sound wave
τ (s)	Signal pluse width
a (m)	Length of the transducer array
b (m)	width of the transducer array
θ_v (°)	Vertical beam angle of the transducer
θ_h (°)	Horizontal beam angle of the transducer

the equivalent plane wave is

$$\mathrm{RL} = 10\lg\left(\frac{I_s}{I_{\mathrm{ref}}}\right) \tag{3}$$

where I_{ref} is the reference sound intensity.

In an ideal seawater medium with a large number of scatterers evenly distributed, the axial sound intensity at the unit distance is I_0 was placed a transmitter with directivity $b(\theta, \emptyset)$. There is a volume scatterer with volume $\mathrm{d}V$ at distance r, its backscattering ability is S'_v, and the definition of scattering intensity is $Sv = 10\lg S'_v$. When the volume element $\mathrm{d}V$ is small enough and the receiving directivity is $b'(\theta, \emptyset)$, the total scattered sound intensity is [19]

$$I_{\mathrm{scat}} = I_0 S'_v \int_V \frac{1}{r^4} \cdot b(\theta, \emptyset) b'(\theta, \emptyset) \mathrm{d}V. \tag{4}$$

According to the definition of equivalent plane wave reverberation level [19], it can be obtained that under the scatterer in the actual ocean is excited by acoustic waves with a pulsewidth of τ, the reverberation level of the equivalent plane wave is

$$\mathrm{RL} = 10\lg\left\{\frac{I_0}{I_{\mathrm{ref}}} \cdot \frac{1}{r^2} \cdot \frac{c\tau}{2} \cdot S'_v \int_\Omega b(\theta, \emptyset) b'(\theta, \emptyset) \mathrm{d}\Omega\right\} \tag{5}$$

where c is the speed of sound and $\mathrm{d}\Omega$ is the solid angle that the cross section of the scatterer opens to the receiving point. Combined with the sound propagation loss in seawater, set the absorption coefficient as α, and the scattering intensity S_v can be calculated by measuring the output voltage of the receiving transducer array

$$S_v = \mathrm{RX} - \mathrm{SRX} - G - \mathrm{SL} + 20\lg r + 2r\alpha - 10\lg\left(\frac{c\tau}{2} \cdot \frac{\theta_v \theta_h \pi}{4}\right). \tag{6}$$

The parameter definitions are shown in Table I.

III. COLD SEEP SONAR SYSTEM

According to the working principle of the cold seep bubble plume and sound wave resonance, the ship-borne cold seep sonar system measures the reverberation level of the equivalent plane wave to achieve the measurement of the active cold seep and water body scattering intensity. The system also forms acoustic images from the echo data [5], [25]. After processing the visual images, it further realizes the identification and detection of seafloor cold seep.

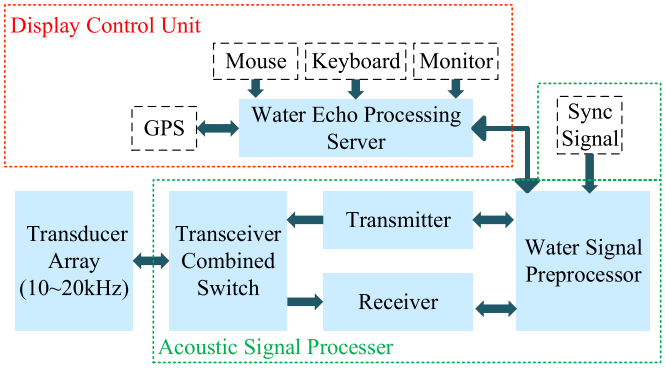

Fig. 2. Structure of display control unit and acoustic signal processor.

Fig. 3. Equipment diagrams of display control unit and acoustic signal processor.

A. System Overview

The system includes three parts: the part of transduce array, the part of the acoustic signal processer and display control unit, and the part of the underwater transducer array.

The structure of the display control unit and the signal processor is shown in Fig. 2, which is placed on the surface boat. The user sets the detection distance, signal form, center frequency, sampling rate, and other parameters on the water echo processing sever through the mouse, keyboard, and monitor. The detection signal is sent through the transducer array after processing by synchronizing, the water echo signal processor, power amplifier, and transmit switch. After the transmit signal reaches the seabed, it is reflected into the transducer array and then returns to the signal processor through the receiving switch and the signal conditioner. Finally, it is spliced into a cold seep image and displayed on the server. The equipment diagrams of the display control unit and the acoustic signal processor are shown in Fig. 3.

The underwater transducer array is installed near the bottom of the ship, which is rigidly connected below the keel and communicates with the signal processer using the watertight cable.

The signal processor transmits measurement sound waves through the transducer array according to the selected frequency, period, pulsewidth, transmission power, and other controllable acoustic parameters. After the transmitter sends out one pulse (i.e., one Ping), the echo data are sampled and recorded at equal time intervals to record the current scattering intensity $S_{v,i}$, which can obtain $\Psi_1, \Psi_2, \ldots, \Psi_i (i = 1, \ldots, N)$, and has a total of N sampling points, as shown in Fig. 4. Under the condition that the sound speed C remains unchanged,

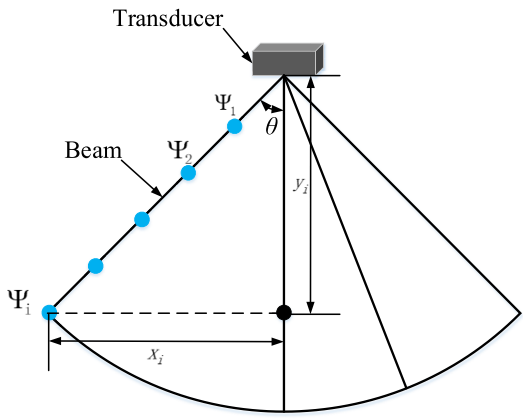

Fig. 4. Schematic of beam sampling point location.

according to the fixed sampling rate Fs of the instrument, the round-trip propagation time of the i_{th} sampling point can be obtained as $T_i = i/Fs$, and the slope distance of the i_{th} sampling point is $\Psi_i = C \times T_i/2 = i \times C/(2 \times Fs)$. According to the directivity θ of the beam, the horizontal track distance x_i and depth y_i of the i_{th} sampling point in the horizontal track-depth coordinate system are obtained as

$$x_i = \Psi_i \sin\theta = \frac{i \cdot C \cdot \sin\theta}{2F}$$
$$y_i = \Psi_i \cos\theta = \frac{i \cdot C \cdot \cos\theta}{2F}. \tag{7}$$

When the transducer emits a single-frequency narrow beam vertically downward, that is, $\theta \approx 0°$, the acoustic section image of the cold seep sonar represents a 2-D plane in which the sampled data are arranged in sequence according to the sampling time. The acoustic section image is defined as: the Ping sampling order is the x-axis, the depth is the y-axis, the scattering intensity $S_{v,i}$ of the sampling points at equal time intervals is the z-axis, and the increasing direction is positive.

B. Frequency Setting

The operating frequency of the sonar has a great influence on the performance of the sonar. When the incident frequency of sound wave resonates with the bubble, the scattering intensity of the target is the highest, and when the frequency is higher than the resonance frequency, the scattering intensity tends to be stable, which is beneficial to the detection of cold seep bubbles in the sea.

According to (6), with the transducer parameters unchanged, only the bubble radius and depth affect the target scattering intensity. Fig. 5 shows the relationship between the resonance frequency and size of bubbles at different depths. When the depth is constant, the resonance frequency increases as the bubble size decreases. For bubbles of the same size, the resonance frequency increases with depth.

The scattering intensity of the bubbles is highly related to the frequency of the incident sound wave, the size of the bubble, and the depth. Fig. 6 presents the plot of the scattering intensity of a single bubble as a function of the incident frequency at different depths and different bubble radii. It can be seen that at the same depth, the larger the bubble radius

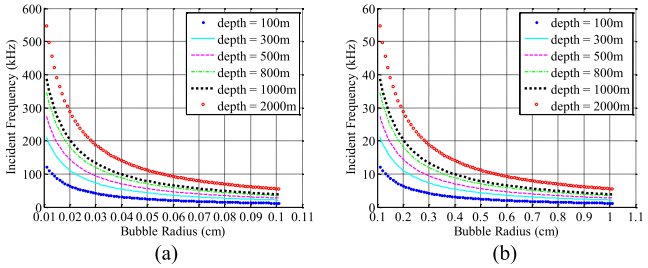

Fig. 5. Evolution of bubble resonance frequency versus bubble radius under different depths. (a) Bubble radius $= 0 - 0.1$ cm. (b) Bubble radius $= 0.1 - 1$ cm.

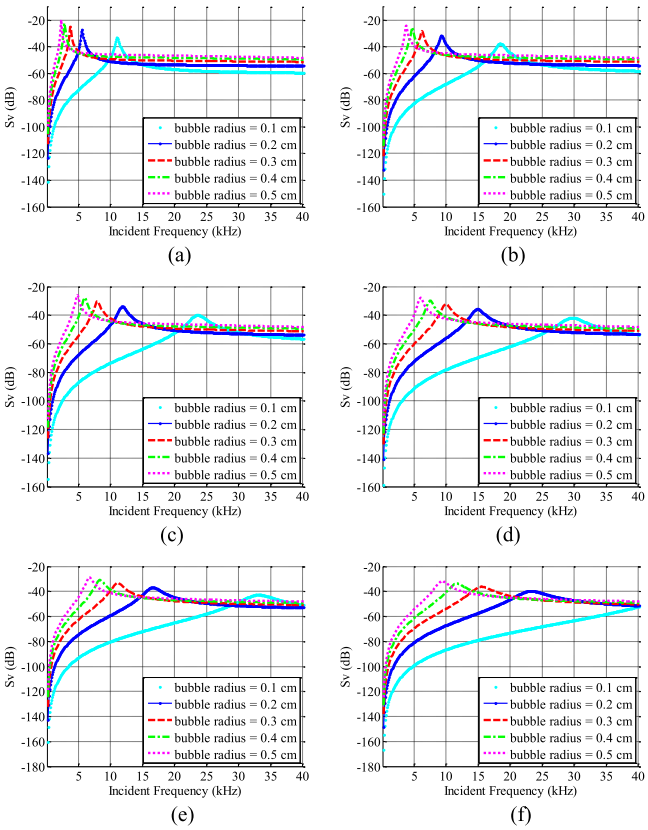

Fig. 6. Evaluation of bubble scattering intensity versus bubble size and incident frequency for different depths. (a) Depth = 100 m. (b) Depth = 300 m. (c) Depth = 500 m. (d) Depth = 800 m. (e) Depth = 1000 m. (f) Depth = 2000 m.

is, the resonance frequency is smaller, and after the incident frequency is greater than the resonance frequency, the target scattering intensity can reach stabilized; under the same bubble radius, when the scattering intensity tends to be stable, the incident frequency increases with the depth.

In summary, in order for sonar to cover more bubbles of different radii in detection, the incident frequency of the cold spring sonar system should be $\geq$10 kHz. In addition, when the incident frequency is $\geq$10 kHz, the scattering intensities at different depths and bubble radii are easy to identify. At the same time, considering the increasing the working frequency, the absorption of the acoustic signal by the seawater will also increase, and the distance detection capability will decrease. Therefore, the working frequency of the cold seep sonar is selected to 10–20 kHz.

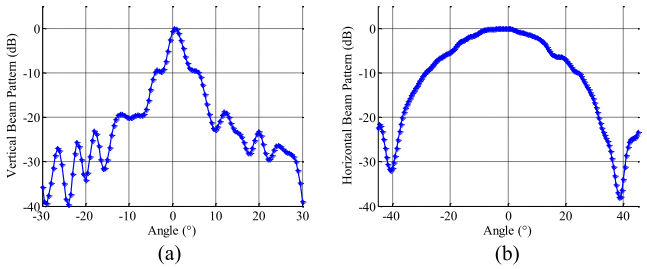

Fig. 7. Beam pattern of the transducer array. (a) Vertical. (b) Horizontal.

C. Transducer Design

The transducer array is used for the transmission and reception of acoustic signals and adopts the design form of a planar array. Its length $a = 10\lambda = 1$ m, width $b = 1.5\lambda = 0.15$ m, and the directivity index $\mathrm{DI} = 10\lg(4\pi S/\lambda^2) = 22.75$ dB; the transmit power of the designed power amplifier $P = 3$ kW and the electroacoustic conversion efficiency $\eta = 0.5$. Therefore, the emitted sound power $P_A = \eta * P = 1.5$ kW.

According to the above parameters, the emission source level of the transducer array can be calculated as

$$\mathrm{SL}_{\max} = 171.8 + 10\lg(P_A) + \mathrm{DI} \approx 226 \text{ dB}. \tag{8}$$

Place the transducer and the standard hydrophone at the same depth underwater, rotate the transducer array horizontally at 2° intervals, and measure the sound source level at different angles. According to the corresponding relationship between the sound source level and the angle, the horizontal beam opening angle can be obtained; in the same way, by changing the pitch angle of the transducer at 2° intervals, the vertical beam opening angle can be obtained. The vertical beam angle of the transducer $\theta_v \approx 5°$, the horizontal beam angle $\theta_h \approx 33°$, and digital weighting is used to suppress the sidelobe. The measured vertical beam and the horizontal beam of the transducer are shown in Fig. 7(a) and (b), respectively.

The operating parameters of the cold seep sonar are shown in Table II.

IV. Cold Seep Sonar Data Processing

A. Data Collection

In the experiment, the cold seep echo data of the acoustic wave at the incident frequency from 14 to 19 kHz were obtained. Using the system, a survey and measurement experiment was carried out in the northern waters of the South China Sea [8], and the measurement range was selected in the cold seep area, where the depth is between 800 and 1300 m. The survey line is centered on the cold seep bubble plume. To reduce the influence of high speed on the measurement results, the speed range of the survey ship is 2.5–5.2 knots during the test. A total of six vertical or intersecting survey lines are designed along the 147° azimuth, and the incident frequencies of 14–19 kHz are used one after another at the six survey lines. Doppler tolerance is considered during cold seep sonar system design. Fig. 8 shows the transducer array design drawing and physical drawing. During operation, the transducer array is fixedly installed on the side of the ship and enters the water 4-m downward.

TABLE II
Sonar Parameters

Frequency (kHz)	Max Power (kW)	Max SL (dB)	DI (dB)	Vertical Beam (°)	Horizontal Beam (°)	Pulse width (ms)
10~20	3	226	23	5	33	0.5~10

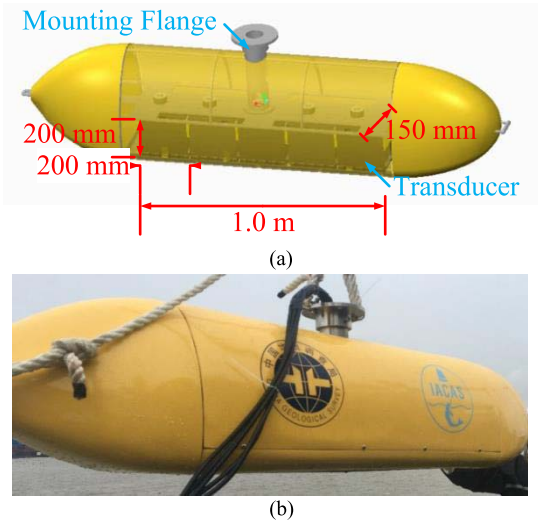

Fig. 8. Transducer array and housing. (a) Design diagram of transducer array. (b) Physical figure of transducer array.

B. Signal Processing

The following signal processing flow is adopted to process the original echo signal in real time: 1) filtering and denoising; 2) Hilbert transform to obtain the signal envelope; and 3) scattering intensity estimation. Considering that different sampling points contain different target scattering intensity values, therefore, the distribution of target scattering intensity is related to the pulse sampling point, the existence of bubbles, and the correct selection of the incident frequency, and the frequency-domain analysis is not necessary. Fig. 9 shows the processing results of the incident signal characterized by a frequency of 15 kHz.

Fig. 9(a) shows the original signal received by the cold seep sonar. Fig. 9(b) shows the filtering result of the original signal, which can significantly reduce the biological noise interference in the deep scattering layer (DSL). Fig. 9(c) shows the envelope of the denoised signal. Fig. 9(d) shows the scattering intensity of each sampling point after compensating for the receiving sensitivity, preamp gain, filter processing gain, and the other parameters of the transducer. Here, the red ellipse marks the scattering intensity generated by the plume, and the green ellipse marks the scattering intensity generated by the seafloor.

The complete scattering intensity of one Ping can be obtained through the above data processing steps. After splicing the scattering intensities of multiple Pings according to the time order, the acoustic section image of size $[N \times M]$ can be obtained, where N represents the number of sampling points per Ping and M represents the total number of Pings.

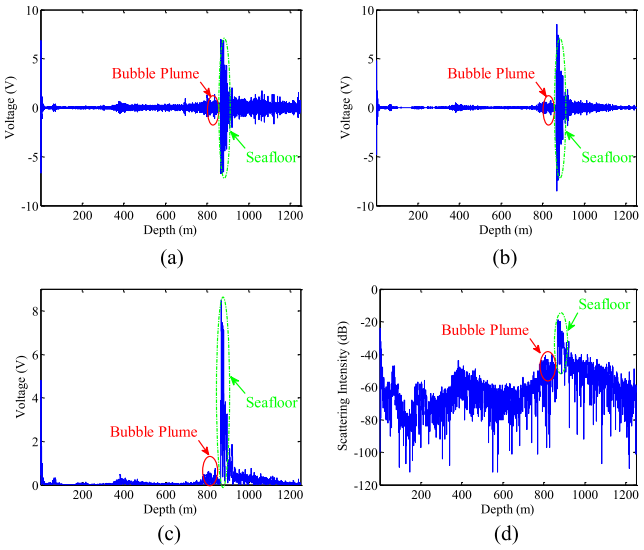

Fig. 9. Sonar echo signal processing results. (a) Original waveform. (b) Filter denoising waveform. (c) Waveform envelope. (d) Scattering intensity distribution.

C. Acoustic Feature Extraction and Recognition

To calculate the scattering intensity accurately of submarine cold seep, recognizing the section image and extracting features of the cold seep are necessary. The essence of the acoustic section image of the submarine cold seep is the grayscale image between 0 and 255, and different targets are distinguished by different brightness.

1) Preprocessing: Since the edge of the bubble plume is not obvious enough compared with the background water body, to highlight the ambiguous edge and improve the contrast between the bubble plume and the water body, homomorphic filtering is used to process the image. The homomorphic filtering is based on the synthetic imaging principle of the amount of source illumination $i(x, y)$ and the reflectance component $r(x, y)$, and the image $f(x, y)$ can be represented [26]

$$f(x, y) = i(x, y)r(x, y). \tag{9}$$

The relative change of $i(x, y)$ in the image $f(x, y)$ is small, which can be seen as the low-frequency component. The reflectance component $r(x, y)$ is the high-frequency component. To eliminate the influence of the uneven distribution of the amount of source illumination, the low-frequency component is reduced, and the high-frequency component is increased in frequency-domain processing, which can achieve the purpose of sharpening the edge. The Gauss high-pass filter is selected as the transfer function of the homomorphic filter

$$H = (f_2 - f_1)\left(1 - e^{\frac{-cD^2}{D_0^2}}\right) + f_1. \tag{10}$$

Here, f_2 and f_1 are adjustment coefficients, representing high-frequency gains and low-frequency gains, respectively; the constant c is used to control the sharpening of the slope; D_0 is the cutoff frequency; and D represents the Euclidean distance of each image pixel from the center of the image

$$D(x, y) = \sqrt{(x - \lfloor M/2 \rfloor)^2 + (y - \lfloor N/2 \rfloor)^2} \tag{11}$$

where $\lfloor * \rfloor$ means round down.

Fig. 10 shows the results of homomorphic filtering for an incident frequency from 14 to 19 kHz. It can be seen that the homomorphic filter can effectively enhance the image part of the bubble plume and make its edge clearer, which provides convenience for observation.

2) Boundary Extraction: As mentioned before, DSL does exist between the sea surface and the seafloor [27], its intensity is lower than the seafloor and the sea surface, about the same as the cold seep bubble, which adversely affects the identification of cold seep. Therefore, the detection and segmentation of the seafloor and the DSL is an important link in the identification of cold seep. The processing of the region growing method is based on the continuity and adjacency between image regions or image regions, that is, an image segmentation algorithm based on the image region feature. Select a point or an area in the image, make it grow according to certain rules, and divide the areas with different feature attributes in the image [28]. Since the seafloor and the DSL have the characteristics of clear and continuous boundaries in the acoustic section image, theoretically, the boundaries can be perfectly segmented by using the regional growth method with a suitable threshold as the growth judgment rule.

Fig. 11 shows the boundary extraction diagram using the region growing method at the incident frequency of 14–19 kHz. The black parts are the seafloor part and the DSL part divided according to the growing rule, and the red lines are the dividing lines extracted based on the growth result. It can be seen that the seafloor and the DSL can be effectively identified, and the boundaries are obvious.

3) Identification: Part of the acoustic section image between the seafloor and the DSL is preserved to eliminate the difficulty in identifying cold seep bubbles caused by the echo intensities. The identification uses the particle swarm optimization algorithm [29]. The basic idea is to find the optimal solution through cooperation and information sharing among individuals in the group.

Since each pixel in the acoustic section image is represented by a gray value from 0 to 255, the initial population number is defined as Θ, the particle position X_k is defined as an array of $[\Theta \times 2]$, and k is the number of iterations, $k = 0, 1, \ldots, K$.

After the iteration starts, first, calculate the probability $\epsilon_m (m = 0, 1, \ldots, 255)$ of each grayscale. The fitness function $F(\xi)$ is defined as

$$F(\xi) = \sum_{0}^{2} \rho_{r,l} \tag{12}$$

$$\rho_{r,l} = \omega_r \cdot \omega_l \cdot (\sigma_r - \sigma_l)^2. \tag{13}$$

Here, $r = 0, 1, 2$; $l = 0, 1, 2$; $r \neq l$; $\xi = 1, 2, \ldots, \Theta$; and ω_0, ω_1, and ω_2 are defined as the probabilities of the acoustic section image in the pixel range $[0, \chi]$, $[\chi+1, \beta]$, and $[\beta+1, 255]$, respectively. $\chi = X_k(\xi, 1)$ and $\beta = X_k(\xi, 2)$. σ_0, σ_1, and σ_2 are defined as the ratio of the expected $E(\mu)$ to the sum of the probability of the acoustic section image in the pixel range $[0, \chi]$, $[\chi + 1, \beta]$, and $[\beta + 1, 255]$, respectively

$$\sigma_\mu = \frac{E(\mu)}{\omega_\mu}. \tag{14}$$

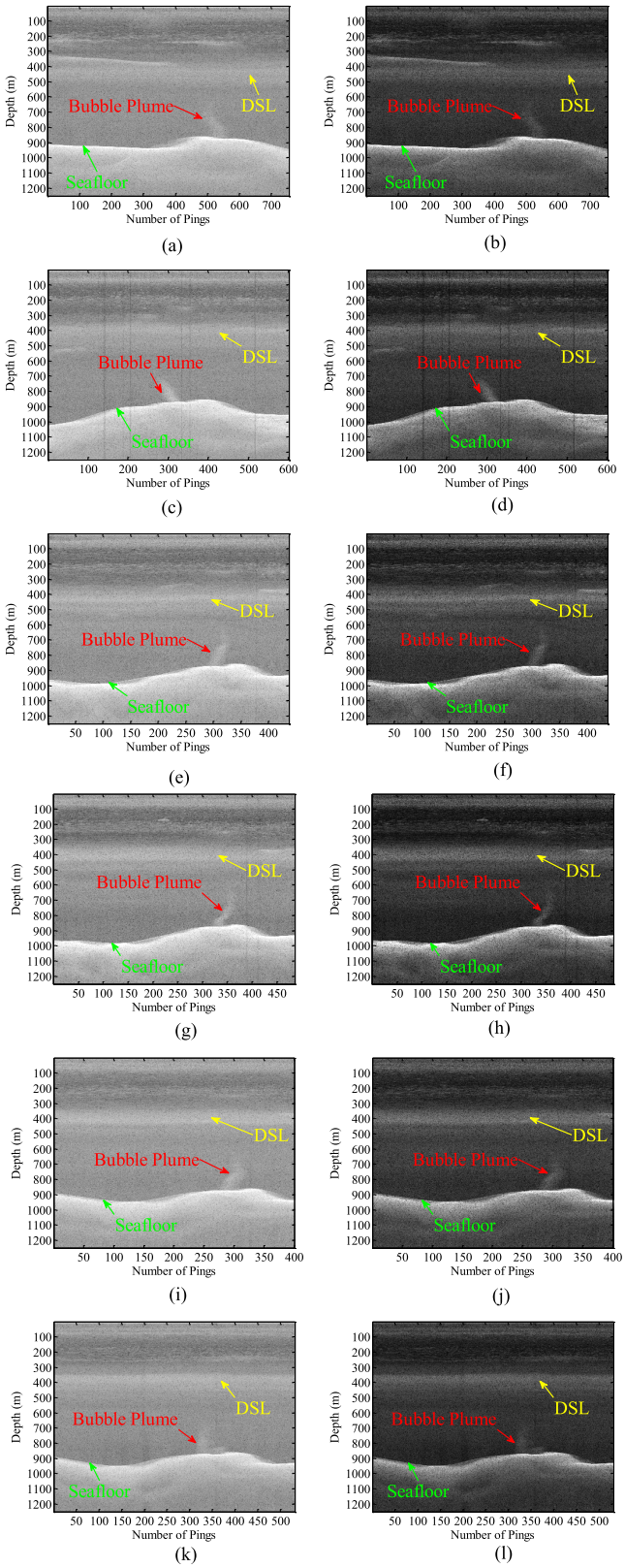

Fig. 10. Preprocessing results of cold seep sonar grayscale image. (a) Original Image of 14 kHz. (b) Homomorphic filtering image of 14 kHz. (c) Original image of 15 kHz. (d) Homomorphic filtering image of 15 kHz. (e) Original image of 16 kHz. (f) Homomorphic filtering image of 16 kHz. (g) Original image of 17 kHz. (h) Homomorphic filtering image of 17 kHz. (i) Original image of 18 kHz. (j) Homomorphic filtering image of 18 kHz. (k) Original image of 19 kHz. (l) Homomorphic filtering image of 19 kHz.

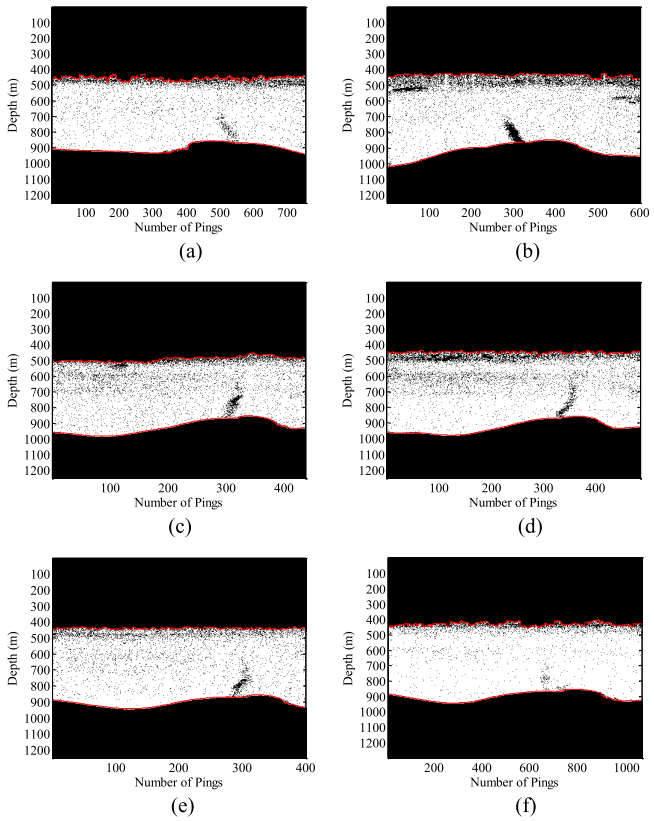

Fig. 11. Extraction results of the seafloor line and the SDL. (a) 14 kHz. (b) 15 kHz. (c) 16 kHz. (d) 17 kHz. (e) 18 kHz. (f) 19 kHz.

Here, $\mu = 1$–3. After K iterations, the optimal position Y_K of the particle swarm is obtained, and the acoustic image of the cold seep can be expressed as

$$\text{Image}_{u,v} = \begin{cases} 255, & \text{Image}_{u,v} \geq Y_k(1,2) \\ \Sigma \dfrac{Y_K}{2}, & Y_K(1,1) < \text{Image}_{u,v} < Y_K(1,2) \\ 0, & \text{Image}_{u,v} \leq Y_K(1,2). \end{cases} \quad (15)$$

After the particle swarm optimization algorithm processes, the cold seep image is represented by up to three values: 0, $\sum Y_K/2$, and 1, which were described as black, gray, and white in the figure, respectively, as shown in Fig. 12, where $K = 200$, and the particle swarm optimization algorithm can accurately identify the cold seep and its shape from the water body.

D. Scattering Intensity Calculation

The measurement of the scattering intensity of the acoustic image was carried out after target identification and feature extraction. According to the signal processing and feature extraction methods presented in Sections IV-B and IV-C, the echo data of the incident acoustic wave at frequencies of 14–19 kHz were processed, and the particle swarm algorithm was used to identify and extract the outline of cold seep bubbles. The processing results are shown in Fig. 13.

After the boundary of the bubble plume is extracted, its echo signal effective values can be calculated, which is directly

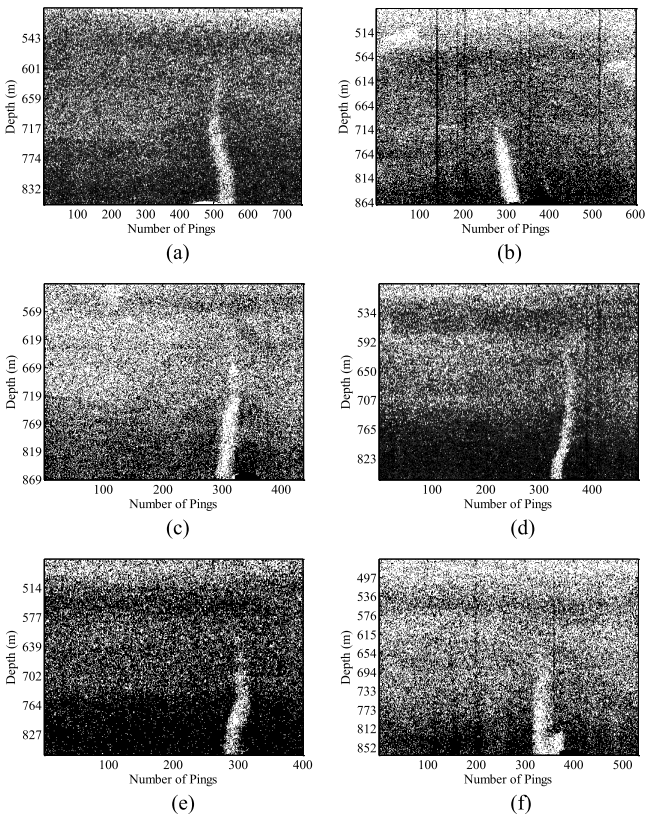

Fig. 12. Cold seep plume identification results. (a) 14 kHz. (b) 15 kHz. (c) 16 kHz. (d) 17 kHz. (e) 18 kHz. (f) 19 kHz.

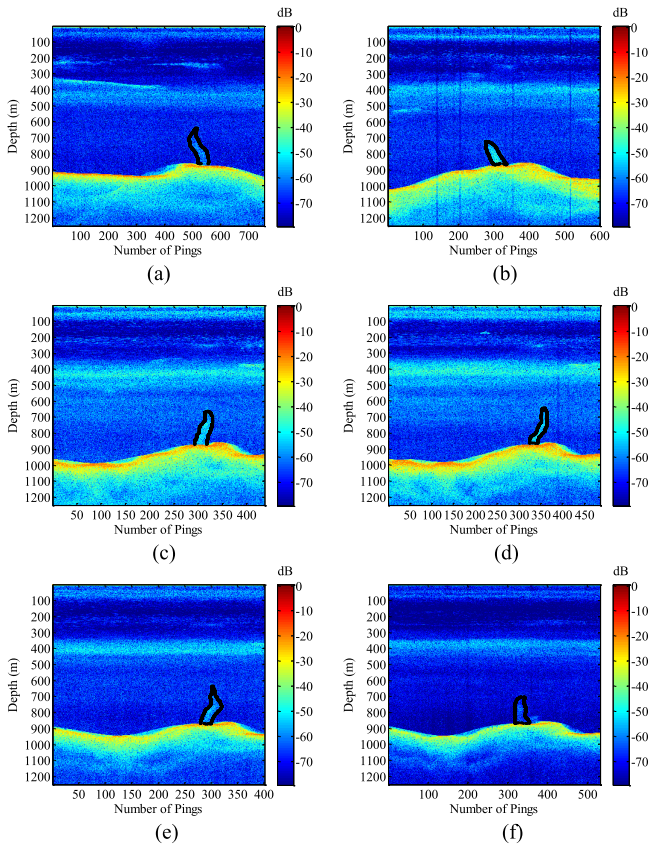

Fig. 13. Cold seep plume contour extraction results. (a) 14 kHz. (b) 15 kHz. (c) 16 kHz. (d) 17 kHz. (e) 18 kHz. (f) 19 kHz.

related to the calculation of target scattering intensity. Analyze the data under the same depth profile at different frequencies so that the effective value of the echo signal is more comparable. Fig. 14 shows the cross-sectional image of the echo signal effective values under the depth ranging from about 700 to 850 m.

The calculation method of the cross-sectional image is to calculate the average value of echo signal effective value in the range of the bubble plume outline at different depths under the same indicate frequency, and next, calculate the target scattering intensity according to the working parameters of the cold seep sonar at different frequencies in the test. In Fig. 14, the x-axis represents the depth of the lateral profile of the plume and the y-axis represents the echo signal voltage. The blue dots represent the effective values of the echo signal, which is related to RX, and the red line represents the fitting result of the effective values of the echo signal. Table III presents the parameter settings of the cold seep sonar at each incident frequency in the detection experiment.

Here, RX is the echo level of the transducer array, SRX is receiving sensitivity of the transducer array, G is the receiver gain, SL is the source level of the acoustic emission signal, $20\lg r$ is the spread loss, $2r\alpha$ is the absorption loss, $10\lg(c\tau/2)$ is the pulsewidth gain, and $10\lg(\theta_v\theta_h\pi/4)$ is the transceiver combined gain. According to (6) presented in Section II-B, the measurement results of the scattering intensity of the cold seep were calculated and compared with the results of theoretical analysis of the acoustic scattering characteristics of the bubble calculated by (2). This comparison is presented in Fig. 15.

TABLE III
SONAR PARAMETERS SETTING

	14 kHz	15 kHz	16 kHz	17 kHz	18 kHz	19 kHz
RX	-15.44	-7.68	-9.78	-10.26	-15.44	-20.63
SRX	-176.3	-176.3	-176.1	-176.9	-177.6	-178.2
G	60	60	60	60	60	60
SL	217.8	218.6	218.1	217.5	216.2	215.7
$20\lg r$	58.58	58.58	58.58	58.58	58.58	58.58
$2r\alpha$	3.32	3.71	4.12	4.55	5.01	5.47
$10\lg(c\tau/2)$	5.74	1.76	3.52	5.74	5.74	5.74
$10\lg(\theta_v\theta_h\pi/4)$	-13.87	-13.87	-13.87	-13.87	-13.87	-13.87
S_v	-46.91	-42.98	-46.13	-47.00	-49.72	-53.35

The blue solid line represents the ideal scattering intensity, where the damping constant of the bubble vibration $\delta = 0$; the red dotted line represents the scattering intensity with strong damping where $\delta = 0.20$, and the black star points represent the scattering intensity measurement results of the cold seep. It can be seen from the figure that the experimental results (black dots) are generally consistent with the distribution of the scattering intensity with damping (red dotted line). In addition, the scattering intensities of theory, damp, and experiment are shown in Table IV, the measurement error, that is, the difference between the experimental scattering intensity and damping scattering intensity is between -3.06 and 0.07 dB,

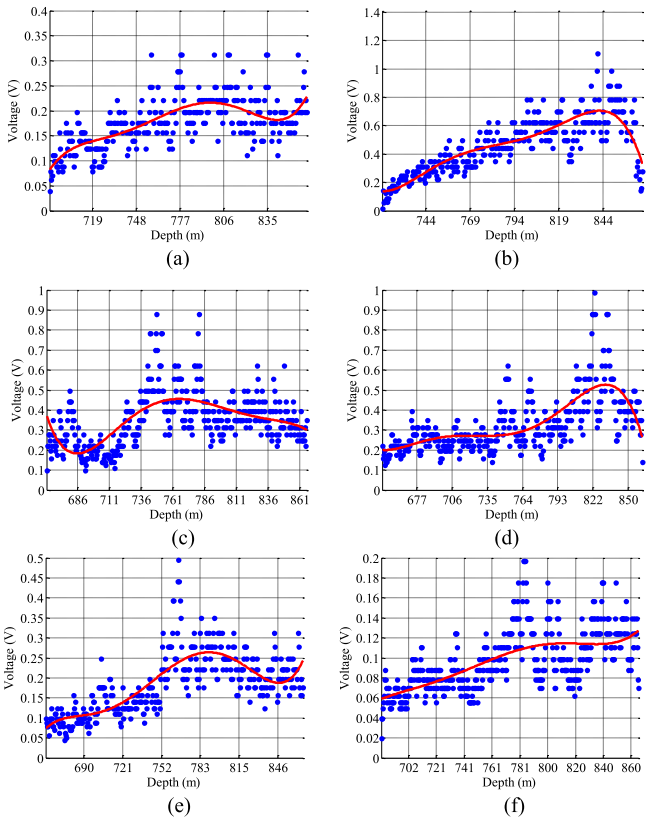

Fig. 14. Cross-sectional image of the echo signal. (a) 14 kHz. (b) 15 kHz. (c) 16 kHz. (d) 17 kHz. (e) 18 kHz. (f) 19 kHz.

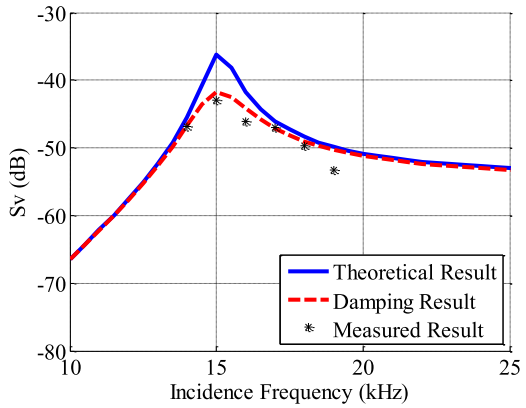

Fig. 15. Theoretical analysis of scattering intensity and comparison of experimental results.

which further verifies that the cold seep bubble has frequency-selective characteristics for the incident acoustic wave, that is, the closer the incident frequency is to the resonance frequency, the larger the scattering cross section, and the stronger the scattering intensity.

Compared with other methods, such as bubble cameras, laser scanning, and quantitative echo sounder carried by the submarine vehicle [1], [30]–[32], the cold seep sonar developed in this article does not need to be carried into the deep sea by the submersible and can be installed on a surface boat to detect the cold spring plume in a wide water area, so it has the advantages of convenience, efficiency, rapid deployment, high integration, and low cost.

TABLE IV
STATISTICS OF SCATTERING INTENSITY

	14 kHz	15 kHz	16 kHz	17 kHz	18 kHz	19 kHz
Theoretical (dB)	-45.45	-36.76	-41.62	-46.00	-48.36	-49.82
Damping (dB)	-46.68	-42.03	-44.13	-47.07	-49.01	-50.29
Experimental (dB)	-46.91	-42.98	-46.13	-47.00	-49.72	-53.35
Error (dB)	-0.23	-0.95	-2.00	0.07	-0.71	-3.06

V. CONCLUSION

The cold seep sonar is designed in this article to measure bubble plume and verify the scattering properties of sound waves by the cold seep bubble. The cold seep located in the northern South China Sea was investigated and measured, and through the processing of the experimental echo data, the cold seep was identified successfully, which can be verified that the bubble has the strongest scattering power and the sonar has the best detection capability when the incident frequency is equal to the resonance frequency. In addition, the measured tests of the incident acoustic wave under the different frequencies were carried out, the experimental results were consistent with the theoretical analysis, and the maximum measurement error is −3.06 dB. This article only identifies the approximate shape of the bubble plume. In the future, other characteristic parameters will be measured or calculated, and the 3-D graphics of the cold seep will be further extracted to provide users with more intuitive cold seep information and realize the acoustic expression of the submarine cold seep. The measurement model also needs to be further modified to adapt to the situation of inhomogeneous cold seep media in the follow-up research. In addition, the cold seep sonar will be optimized and miniaturized to make it more portable and easier to install.

REFERENCES

[1] C. Aoyama *et al.*, "Acoustical surveys of methane plumes using the quantitative echo sounder in Japan sea," in *Proc. Symp. Underwater Technol. Workshop Sci. Submarine Cables Rel. Technol.*, Apr. 2007, pp. 249–255, doi: 10.1109/UT.2007.370804.

[2] A. Joseph, *Investigating Seafloors and Oceans*. Amsterdam, The Netherlands: Elsevier, 2017.

[3] W. Zhao *et al.*, "Discussion on the submarine bubble plume and its effect on hydrocarbon resources," *Prog. Geophys.*, vol. 36, no. 5, pp. 2251–2263, 2021, doi: 10.6038/Pg2021EE0366.

[4] R. Kubilius and G. Pedersen, "Relative acoustic frequency response of induced methane, carbon dioxide and air gas bubble plumes, observed laterally," *J. Acoust. Soc. Amer.*, vol. 140, no. 4, pp. 2902–2912, Oct. 2016, doi: 10.1121/1.4964250.

[5] Y. Yu *et al.*, "Research on acoustic detection parameters for bubble plume in cold seeps," *Mar. Geol. Quaternary Geol.*, vol. 39, no. 2, pp. 188–199, 2019, doi: 10.16562/J.cnki.0256-1492.2018042401.

[6] J. Greinert and B. Nutzel, "Hydroacoustic experiments to establish a method for the determination of methane bubble fluxes at cold seeps," *Geo-Mar. Lett.*, vol. 24, no. 2, pp. 75–85, 2004, doi: 10.1007/S00367-003-0165-7.

[7] I. Dumke *et al.*, "Sidescan backscatter variations of cold seeps on the Hikurangi margin (New Zealand): Indications for different stages in seep development," *Geo-Mar. Lett.*, vol. 34, nos. 2–3, pp. 169–184, 2014, doi: 10.1007/S00367-014-0361-7.

[8] B.-R. Liu *et al.*, "Characteristics and formation mechanism of cold seep system in the northeastern continental slope of south China sea from sub-bottom profiler data," *Chin. J. Geophys.-Chin. Ed.*, vol. 58, no. 1, pp. 247–256, 2015, doi: 10.6038/cjg20150122.
[9] I. Klaucke *et al.*, "Acoustic investigation of cold seeps offshore Georgia, eastern Black Sea," *Mar. Geol.*, vol. 231, nos. 1–4, pp. 51–67, Sep. 2006, doi: 10.1016/J.margeo.2006.05.011.
[10] I. Klaucke, W. Weinrebe, C. J. Petersen, and D. Bowden, "Temporal variability of gas seeps offshore New Zealand: Multi-frequency geoacoustic imaging of the Wairarapa area, Hikurangi margin," *Mar. Geol.*, vol. 272, nos. 1–4, pp. 49–58, Jul. 2010, doi: 10.1016/j.margeo.2009.02.009.
[11] A. T. Jones *et al.*, "Acoustic and visual characterisation of methane-rich seabed seeps at Omakere Ridge on the Hikurangi margin, New Zealand," *Mar. Geol.*, vol. 272, nos. 1–4, pp. 154–169, Jul. 2010, doi: 10.1016/j.margeo.2009.03.008.
[12] X. Tu *et al.*, "Study on the impact of bubble curtain on underwater acoustic communication," in *Proc. Oceans Taipei*, 2014, pp. 1–5, doi: 10.1109/OCEANS-TAIPEI.2014.6964397.
[13] V. A. Akulichev and V. A. Bulanov, "Acoustical nonlinearity, sound absorption, and scattering in bubble-saturated seawater," *Doklady Earth Sci.*, vol. 479, no. 1, pp. 375–378, Mar. 2018, doi: 10.1134/S1028334x18030133.
[14] R. Y. Nishi, "Scattering and absorption of sound-waves by a gas bubble in a viscous-liquid," *Acustica*, vol. 33, no. 2, pp. 65–74, 1975.
[15] Y. Jiawen *et al.*, "Influence of softening effect of bubble water on cavity resonance," in *Proc. OES China Ocean Acoust. (COA)*, 2021, pp. 351–355, doi: 10.1109/COA50123.2021.9519925.
[16] Z. Qun and Y. Wang, "Obtaining the resonant frequency of the bubble in the ship wake by ANSYS," in *Proc. 7th Int. Conf. Comput. Intell. Secur.*, Dec. 2011, pp. 812–816, doi: 10.1109/CIS.2011.184.
[17] W. S. Burdic and J. F. Bartram, "Underwater acoustic system analysis by William S. Burdic," *J. Acoust. Soc. Amer.*, vol. 76, no. 3, p. 996, 1984, doi: 10.1121/1.391242.
[18] R. J. Urick, *Principles of Underwater Sound*, 3rd ed. New York, NY, USA: McGraw-Hill, 1983.
[19] R. G. Holt and L. A. Crum, "Acoustically forced oscillations of air bubbles in water: Experimental results," *J. Acoust. Soc. Amer.*, vol. 91, no. 4, pp. 1924–1932, Apr. 1992, doi: 10.1121/1.403703.
[20] A. E. A. Blomberg, T. O. Saebo, R. E. Hansen, R. B. Pedersen, and A. Austeng, "Automatic detection of marine gas seeps using an interferometric sidescan sonar," *IEEE J. Ocean. Eng.*, vol. 42, no. 3, pp. 590–602, Jul. 2017, doi: 10.1109/JOE.2016.2592559.
[21] B. Nutzel and H. Herwig, "A two-frequency hydroacoustic scatterometer for bubble scattering investigations," *IEEE J. Ocean. Eng.*, vol. 19, no. 1, pp. 41–47, Jan. 1994, doi: 10.1109/48.289449.
[22] D. R. Palmer, "Acoustical scattering from constituents of an ocean plume located near a boundary surface," *IEEE Trans. Geosci. Remote Sens.*, vol. 43, no. 4, pp. 770–777, Apr. 2005, doi: 10.1109/TGRS.2005.844309.
[23] M. V. Trevorrow, S. Vagle, and D. M. Farmer, "Acoustical measurements of microbubbles within ship wakes," *J. Acoust. Soc. Amer.*, vol. 95, no. 4, pp. 1922–1930, Apr. 1994, doi: 10.1121/1.408706.
[24] S. Vagle and D. M. Farmer, "The measurement of bubble-size distributions by acoustical backscatter," *J. Atmos. Ocean. Technol.*, vol. 9, no. 5, pp. 630–644, 1992, doi: 10.1175/1520-0426(1992)009<0630:Tmobsd>2.0.Co;2.
[25] L. Guo *et al.*, "The research of deep-sea water scattering strength measurement technology," in *Proc. IEEE/OES China Ocean Acoust. (COA)*, Jan. 2016, pp. 1–3, doi: 10.1109/COA.2016.7535813.
[26] M. Tiwari and B. Gupta, "Brightness preserving contrast enhancement of medical images using adaptive gamma correction and homomorphic filtering," in *Proc. IEEE Students' Conf. Electr., Electron. Comput. Sci. (SCEECS)*, Mar. 2016, pp. 1–4, doi: 10.1109/SCEECS.2016.7509287.
[27] L. Feng *et al.*, "Deep scattering layer observation by acoustic correlation current profiler," in *Proc. Oceans MTS/IEEE Kobe Techno-Ocean*, Apr. 2008, pp. 1–4, doi: 10.1109/OCEANSKOBE.2008.4531031.
[28] J. Duan and Q. Bai, "Cell image processing based on distance transform and regional growth," in *Proc. 5th Int. Conf. Internet Comput. Sci. Eng.*, Nov. 2011, pp. 6–9, doi: 10.1109/ICICSE.2010.20.
[29] A. Ahilan *et al.*, "Segmentation by fractional order Darwinian particle swarm optimization based multilevel thresholding and improved lossless prediction based compression algorithm for medical images," *IEEE Access*, vol. 7, pp. 89570–89580, 2019, doi: 10.1109/ACCESS.2019.2891632.
[30] H. Mizushima *et al.*, "Autonomous recognition of bubble plumes for navigation of underwater robots in active shallow vent areas," in *Proc. Oceans*, 2007, pp. 1–6, doi: 10.1109/OCEANS.2007.4449284.
[31] M. D. Stokes and G. B. Deane, "A new optical instrument for the study of bubbles at high void fractions within breaking waves," *IEEE J. Ocean. Eng.*, vol. 24, no. 3, pp. 300–311, Jul. 1999, doi: 10.1109/48.775292.
[32] T. Xue, L. Xu, Q. Wang, B. Wu, and J. Huang, "A 3-D reconstruction method of dense bubbly plume based on laser scanning," *IEEE Trans. Instrum. Meas.*, vol. 69, no. 5, pp. 2145–2154, May 2020, doi: 10.1109/TIM.2019.2922753.

Lin Guo received the M.S. degree in underwater acoustic engineering from Harbin Engineering University, Harbin, China, in 2005, where he is currently pursuing the Ph.D. degree with the College of Underwater Acoustic Engineering.

Since graduation, he has been with the Shanghai Acoustics Laboratory, Chinese Academy of Sciences, Shanghai, China. He has dedicated himself to the field of ocean engineering and ocean acoustics. His current research interests include underwater acoustic positioning technology, underwater acoustic detection technology, and underwater acoustic communication technology.

Octavian Postolache (Senior Member, IEEE) received the Ph.D. degree in electrical engineering from UTI, Iasi, Romania, in 1999, and the Habilitation degree from the Instituto Superior Tecnico, Universidade de Lisboa, Lisbon, Portugal, in 2016.

He is currently a Professor with ISCTE–IUL, Lisbon, and a Senior Researcher with the Instituto de Telecomunicacoes, Lisbon. He acts as an Active Coordinator or a member of national and international research projects particularly Portuguese and EU projects. He has authored or coauthored ten patents, ten books, 18 book chapters, and more than 400 papers in international journals and proceedings of international conferences with peer-to-peer review. His current research interests include smart sensors and the Internet of Things (IoT) for biomedical, environmental, and precision agriculture applications; intelligent transportation; wireless sensor networks and visual senor networks; and artificial intelligence applied automated measurement systems.

Dr. Postolache is active on IEEE organization, where he serves as the Chair for IEEE IMS TC13 and IEEE IMS Portugal chapter.

Lin Ma received the M.Sc. degree in telecommunications and computer engineering from ISCTE-Instituto Universitário de Lisboa, Lisbon, Portugal, in 2019.

Since 2020, she has been with the Shanghai Acoustics Laboratory, Chinese Academy of Sciences, Shanghai, China. Her current research interests include acoustic signal processing and underwater acoustic positioning navigation technology.

Yang Shi received the M.S. degree in communication and information system from Harbin Engineering University, Harbin, China, in 2006, where she is currently pursuing the Ph.D. degree with the College of Underwater Acoustic Engineering.

Since graduation, she has been with the Shanghai Acoustics Laboratory, Chinese Academy of Sciences, Shanghai, China. Her current research interests include underwater acoustic positioning, detection, and communication technology.